# FORECASTING GEOMAGNETIC AND SOLAR ACTIVITY BASED ON MACROSCOPIC NONLOCAL CORRELATIONS

**© 2025 S.M. Korotaev [a, *], V.O. Serdyuk [a], E.O. Kiktenko [a], I.V. Popova [a], N.M. Budnev [b], Yu.V. Gorokhov [c]**

[a1] *Geoelectromagnetic Research Center, Schmidt Institute of Physics of the Earth, Russian Academy of Sciences (GEMRC IPE RAS), Moscow, Troitsk, Russia*

[b] *Irkutsk State University (ISU), Irkutsk, Russia*

[c] *Pushkov Institute of Terrestrial Magnetism, Ionosphere and Radio Wave Propagation, Russian Academy of Sciences (IZMIRAN), Moscow, Troitsk, Russia*

* *e-mail : korotaev@gemrc.r u*

Received August 13, 2024

Revised September 09, 2024

Accepted for publication September 26, 2024

A series of long-term experiments studying macroscopic nonlocal correlations between random dissipative heliogeophysical processes and probe processes in detectors revealed important properties of macroscopic entanglement predicted by absorption electrodynamics. These correlations have retarded and advanced components. The advanced correlation corresponds to reverse-time causality (due to the randomness of processes, this does not lead to well-known paradoxes). The dominant global source processes causing detector responses turned out to be solar and geomagnetic activity. Advanced correlations enable forecasting of random components of these processes. The practical feasibility of such forecasts with a lead time of several months and with accuracy , sufficient for all practical purposes is demonstrated.

**DOI:** 10.31857/S00167940250208e8

## 1. INTRODUCTION

Advanced (backward-time) quantum nonlocal correlations follow from various theoretical considerations, and their existence is confirmed in relevant experiments [Elitzur and Dolev, 2003; Laforest et al., 2006; Lloyd et al., 2011; Ma et al., 2012; Megidish et al., 2013]. A universal interpretation of symmetric retarded and advanced correlations is given based on the Wheeler - Feynman absorption electrodynamics [Cramer, 1980, 1986]. The most interesting is the observation of nonlocal correlations at the macroscopic level, where time shifts due to slow diffusion exchange of entanglement can be very large, making the prognostic application of the advanced component possible. In experiments studying nonlocal correlations of large-scale random dissipative processes,

we relied on the macroscopic entanglement equation, which connects entropy production in the probe process-detector and in the source process with positive and negative time shifts. In the mid-1990s, the first long-term experiment was initiated at the laboratory facility in Troitsk, aimed at establishing correlations between natural source processes and test processes in different types of detectors completely isolated from classical local influences, and subsequently, investigating the possibilities of their prognostic applications. Since 2012, a similar but broader experiment has been conducted in parallel at a deep-water facility based at the Baikal Neutrino Observatory. The number of natural dissipative source processes causing a noticeable response in detectors is small due to the monogamy property of quantum correlations. The dominant global source turned out to be solar activity, while geomagnetic activity proved to be weaker but well distinguishable. Both experiments are ongoing at present.

In this paper, we summarize the results of these experiments, prefacing them with a brief outline of the theoretical basis and instrumental implementation, then focusing on data analysis in their prognostic aspect.

## 2. MACROSCOPIC NONLOCAL CORRELATIONS OF DISSIPATIVE P ROCESSES

Although at the beginning of the development of quantum information physics it was believed that the phenomenon of entanglement and, accordingly, nonlocal correlations could only be observed at the micro level, it was soon shown that this is not the case [Home and Majumdar, 1995]. Macroscopic quantum entanglement is currently the subject of a growing stream of research (for example, [Amico et al. 2008; Kordas et al., 2012; Reid et al., 2012; Maldacena and Susskind, 2013; Lee et al., 2015]). A key role was played by the discovery of the constructive role of dissipation in generating weak, but leading to experimentally observable effects, natural entanglement of macrosystems. Due to the complexity of the phenomenon, a rigorous theoretical description is available so far only for a few special cases. However, in the experiment, one can be guided by a general, although admittedly approximate, equation of macroscopic entanglement, based on the arguments of absorption electrodynamics [Korotaev, 2011; Korotaev and Morozov, 2018]:

$$\dot{S}_d = \sigma \int \frac{\dot{s}}{x} \delta\left(v^2 t^2 - x^2\right) dV \,, \tag{1}$$

where $\dot{S}_d$ is the entropy production per particle in the probe process (detector) ; $\dot{s}$ is the density of total entropy production in the sources, the integral is taken over the four-dimensional volume of sources ; $\sigma$ is the transaction cross-section (of the order of the atom cross-section and tends to zero

in the classical limit): $\sigma \approx \hbar^4 / m_e^2 e^4$ ; $m_e$ is the electron mass ; $\delta$ function shows that processes correlate with symmetric delay and advancement. The propagation velocity $v$ for diffusion exchange of entanglement can be very small. Accordingly, the delay and advancement can be large.

A detector can be some dissipative random process isolated from classical local influences. The developed theory of several types of detectors allows connecting entropy production in the test process with the measured signal; similarly, entropy production in the source process can be connected with a suitable index of its activity. This made it possible to test equation (1) not only theoretically (on a spin gas model [Calsamiglia et al., 2005]), but also experimentally (based on calculating entropy production during ohmic dissipation of currents from the source of geomagnetic variations *Dst* ) [Korotaev, 2011; Korotaev and Morozov, 2018]. In practice, however, it is simpler to study the correlation of the detector signal directly with the source activity index.

Equation (1) in its simplest form does not account for absorption by the intermediate medium. Its influence, however, is qualitatively quite remarkable. In [Hoyle and Narlikar, 1995], it is proven that although the equations of absorption electrodynamics are time-symmetric, its fundamental asymmetry manifests through asymmetry in absorption efficiency: absorption of retarded field is complete, while advanced field absorption, in contrast, must be incomplete. This leads to the fact that the level of the advanced component of nonlocal correlations through a screening medium can be higher than the retarded one.

## 3. EXPERIMENTAL TECHNIQUE

Although, generally speaking, any dissipative process can be used as a probe, its actual choice is dictated by the relative magnitude of the effect and theoretical "transparency," allowing to connect the measured macroparameter (signal) with the left side of (1) and consciously take measures to shield and/or control all possible local noise-generating factors (temperature, pressure, local electromagnetic field, etc.). Based on these considerations, three types of detectors were selected: the first is based on spontaneous fluctuations of weakly polarizing electrodes in an electrolyte, the second on spontaneous fluctuations of dark current in a photomultiplier (in other words, both are based on measuring spontaneous fluctuations in the height of the potential barrier), and the third on fluctuations in the mobility of ions in a small volume of electrolyte (in an electrolytic cell). Two experimental setups were created: TsGEMI-IZMIRAN (Troitsk) with detectors of the first two types and MGTU (Moscow) setup with detectors of the third type. In both setups, comprehensive measures have been taken to shield and/or control and mathematically account for (if complete

shielding is impossible) all possible classical local influences for each detector [Korotaev, 2011; Korotaev and Morozov, 2018]. Experience has shown that electrode-type detectors are the most reliable in long-term experiments. The requirement for long experiment duration stems from the fact that macroscopic nonlocal correlations manifest at extremely low frequencies (at periods of about a month or more).

The main problem of the experiment, which dictates the detector design and primary signal processing, lies in the necessity of instrumental or mathematical exclusion of all possible local influences on the detector signal. These issues, as well as other metrological characteristics of the setup , are detailed in the works [Korotaev, 2011; Korotaev and Morozov, 2018; Korotaev et al., 2024]. Here, due to the context of the article, we only separately emphasize the complete absence of detector response, within its sensitivity limits, to a local magnetic field up to 1 mT in the range 0–1 Hz . Furthermore, it has been established that the correlation of the detector signal with cosmic ray flux is significantly weaker than directly with indices of geomagnetic and solar activity. A simplified diagram of the first electrode detector based on marine low-polarization graphite-manganese electrodes is shown in Fig. 1.

Fig. 1.

In 2009, the TsGEMI-IZMIRAN installation was modified, the electrode detector was replaced with a new one based on silver-silver chloride high-quality metrological marine low-polarization electrodes KhD-5.519.00, produced in a single small series by the "Etalon" factory (Kyiv). These electrodes were developed for precision measurements of constant electric field in the sea and are the best in the world in terms of insensitivity of their own potentials to physicochemical environmental conditions. In addition , the hardware and software channel for accounting for temperature influence has been improved, taking into account the nonlinearity and non-stationarity of this influence [Korotaev and Morozov, 2018; Korotaev et al., 2024].

In 2012, a new experiment was simultaneously launched based on the Baikal Deep Underwater Neutrino Observatory of the INR RAS. Baikal is the deepest lake in the world , and its powerful and calm water layer provides good protection against classical local influences. In particular, at a depth of just a few dozen meters, natural temperature stabilization proves better than what can be achieved in ordinary laboratory conditions, and at the bottom, the temperature remains constant with an accuracy of 0.01 K. On the other hand, measurements with detectors at large vertical separation can be easily implemented in the water column of Lake Baikal, which allows testing the assumption about the dominance of external (heliogeophysical) processes that non-locally affect detectors. Synchronous measurements with the CGEMI-IZMIRAN ground laboratory

installation, located 4200 km away, should both verify the planetary nature of non-local correlations with global sources and help identify regional sources (particularly earthquakes), the study of which was also included in the experimental program. The deep-water installation uses pairs of HD-5.519.00 electrodes as detectors, identical to those used in the laboratory installation. Two such pairs are located at the near-bottom and near-surface horizons. Additionally, the installation is used for monitoring the classical electric field on the surface-bottom baseline **.** A detailed description of the deep-water installation is provided in the works [Korotaev et al., 2015; Korotaev and Morozov, 2018; Korotaev et al., 2018b].

Fig. 2.

The installation is completely autonomous, located 10 km from the shore at a depth of 1367 m; its simplified diagram is shown in Fig. 2. The lower detector (signal *Ub* ) is placed at a depth of 1337 m, the upper one (signal *Ut* ) at 47 m, the electronics unit at 20 m, and the submerged buoy at 15 m. The installation operates in annual cycles: in March of each year, it is partially or completely raised onto the ice for data retrieval and technical maintenance.

## 4. DATA ANALYSIS METHODOLOGY

The data were processed using spectral, correlation and causal analysis methods. Let us recall the essence of the latter. For any variables $x$ and $y$ , one can define in terms of Shannon's unconditional $S(x)$, $S(y)$ and conditional $S(x|y)$, $S(y|x)$ entropies, the independence functions:

$$i_{y|x} = \frac{S(y \mid x)}{S(y)},\ i_{x|y} = \frac{S(x \mid y)}{S(x)},\ 0 \le i \le 1. \quad (2)$$

Roughly speaking, independence functions behave inversely to the modulus of the correlation function. However, they characterize one-sided correlations that are asymmetric for causally related variables. In addition, they are equally suitable for any linear and nonlinear relationships. The causality function is considered below. g is considered:

$$\gamma = \frac{i_{y|x}}{i_{x|y}},\ 0 \le \gamma < \infty. \quad (3)$$

By definition $x$ is the cause and $y$ is the effect if $\gamma < 1$ . Conversely, $y$ is the cause and $x$ is the effect if $\gamma < 1$ . The physical meaning of this formal definition consists in stating the irreversible loss of information during a causal transition.

In terms of γ, the principle of classical causality is formulated as follows:

$$\gamma < 1 \Rightarrow \tau > 0,\ \gamma > 1 \Rightarrow \tau < 0,\ \gamma \to 1 \Rightarrow \tau \to 0\ ,$$

(4)

Where τ is the time shift of $y$ relative to $x$ . Only in the case of nonlocal correlations can a violation of this principle be observed. This is precisely the case of weak causality [Cramer, 1980], which does not obey the combination of inequalities (4). Violation of inequalities (4) is evidence (a sufficient condition) of entanglement, that is, evidence of the nonlocal nature of correlations. This is not the only possible evidence of entanglement; along with it, in the analysis of the described experiments, we used a more traditional approach that does not appeal to time shifts – violation of the steering inequality [Korotaev, 2011; Korotaev and Morozov, 2018; Korotaev et al., 2018a]. But violation of (4) – reverse-time causality (emphasizing that, due to the randomness of processes, it does not lead to any paradoxes) – is more adequate evidence in the predictive context [Korotaev et al., 2005, 2018a, 2018b, 2020, 2022; Korotaev, 2011; Korotaev and Morozov, 2018].

The slow random component of solar activity is most prominently expressed in intermittent oscillations, occupying a range of quasi-periods of approximately 50-500 days [Lean and Brueckner, 1989]. The random component of geomagnetic activity occupies the same range, but it is somewhat more difficult to isolate, since deterministic components - annual variation and its harmonics - also lie within this range.

As an index of solar activity, the radio emission flux $R$ is used. It turned out that the maximum of the correlation function of the detector signal $U$ with $R$ (and the minimum of the independence function $U$ from $R$ ) are observed in the frequency range $R$ 610-2800 MHz. It is noteworthy that this range corresponds to radiation from the upper chromosphere-lower corona - the layer of maximum entropy production in the solar atmosphere [Korotaev, 2011; Korotaev and Morozov, 2018]. Comparable, but usually lower correlation , is observed with X-ray radiation. As a measure of geomagnetic activity, we have adopted the *Dst* -index .

Optimal broadband filtering for isolating random components in time series is sought based on the similarity of current spectra. This procedure is described in numerous examples in [Korotaev et al., 2005, 2018a, 2018b, 2019, 2020, 2022; Korotaev, 2011; Korotaev and Morozov, 2018; Korotaev et al., 2019] .

## 5. RESULTS

Figure 3 presents an example of the causal analysis results of the electrode detector signal from the TSGEMI-IZMIRAN installation and solar activity. In the leading region ( $\tau > 0$ ) the values of the independence functions $U$ from $R$ are significantly lower than in the lagging region ( $\tau > 0$ ), and the causality function is significantly greater than 1. The global minimum $i_{U|R} = 0.47^{+0.02}_{-0.01}$ and global maximum $\gamma = 1.58 \pm 0.03$ are observed at $\tau = 42$ days. Violation of inequality (4) indicates the nonlocal nature of the correlation.

Fig. 3., Fig. 4.

In Fig. 4, the result is presented in terms of the correlation function. The main maximum $r_{UR} = 0.51 \pm 0.02$ is observed with a lead of $\tau = 42$ days, in agreement with the causal analysis result.

Fig. 5.

Figure 5 shows the correlation function of the detector signal and geomagnetic activity, also demonstrating a global $\max r_{UDst} = 0.70 \pm 0.02$ at $\tau = 42$ days.

Such correlations allow solving prognostic tasks. Among various mathematical approaches, the method of current impulse response function was the first and quite successful one, taking into account the non-Markovian nature of the process in a piecewise linear approximation. On the training interval, $[t_1, t_2]$ the impulse response function $g(\tau)$ is calculated, which connects the detector signal $X$ and the predicted parameter $Y$ , by solving the integral equation:

$$Y(t) = \int_{t_1}^{t_n} g(\tau) X(t-\tau) d\tau \ .$$

(5)

The complete training interval $Y$ ends with the last observed value, and $X$ is preceded by $\Delta t$ . The impulse response function found by solving the inverse problem is used on the next interval of detector signal data, ending in the last measured value, and one value $Y$ is predicted with a lead time $\Delta t$ . Thus, the direct problem (5) is solved on the interval $X$ , ending with the last observed value. At the next step, the training interval is pulled forward by one discrete, the procedure is repeated, and the next value $Y$ is predicted. This minimizes the influence of non-stationarity and nonlinearity. The stability of the result, if necessary, is improved by optimal low-frequency post-filtration (at the cost of a slight decrease in lead time). A detailed description of the method

implementation and its discussion are provided in the works [Korotaev et al., 2007; Korotaev, 2011; Korotaev and Morozov, 2018].

Fig. 6, Fig. 7.

Figures 6 and 7 show the results of long-term daily series of forecasts *R* and *Dst* with a fixed lead time corresponding to the time shift (42 days) of the global correlation maximum. The actual lead time is slightly less than this shift due to post-filtration. The different start times of the forecasts for *R* and *Dst* are related to different optimal pre-filtration of the pairs *U-R* and *U-Dst* , which differently reduce the original series.

Unfortunately, the position of the global correlation maximum changes significantly over time, and no pattern of this variability has been found yet. Although physical modeling indicates an inverse relationship between this time and the source energy [Korotaev et al., 2019], in the results of the field experiment this appears as no more than a tendency. Thus, according to a series of measurements about eight years later, the global correlation maximum *U* both with *R* (0.92±0.02) and with *Dst* (0.87±0.04) occurred at a lead time of 130 days. The forecasting results (with a reduced lead time of 123 days due to post-filtering) are shown in Figures 8 and 9.

Fig. 8. Fig. 9.

The Baikal deep-water experiment provides higher quality data compared to the laboratory experiment, but the data is obtained in series of about a year in length, which for methodological reasons can almost never be combined into a longer series. Meanwhile, for any self-learning forecasting algorithms, the length of the series should be much greater than the optimal lead time of the forecast (determined by the observed time shift of the correlation function). At the same time, the length of the series is always significantly reduced by the applied optimal broadband filtering. In the tasks of the Baikal experiment , related to the forecast of relatively small-scale regional processes, for which the time shifts are small, the duration of the obtained series is sufficient for their successful solution. For solar-geomagnetic forecasts, this is not yet possible (until the planned commissioning in 2025 of a new deep-water installation allowing continuous measurements of unlimited duration).

However, high correlation with solar activity is always observed in underwater data. Note that of the two detectors: upper *Ut* and lower *Ub* , local interferences are minimal in the lower one, but at the same time, the useful signal in it is also lower due to shielding by the overlying water column. As a result, the signal-to-noise ratio in them is comparable; in years of high activity, it is higher for *Ub* , in years of low activity – for *Ut* .

Although due з to the limitation of the series, a real quantitative forecast is not available, it is easy to qualitatively demonstrate its possibility by simply shifting the filtered series. An example for a series where the global maximum correlation equals 0.95±0.02 with *Ut* leading *R* by 180 days is shown in Fig. 10.

Fig. 10, Fig. 11.

It is more difficult to do something similar with short series for geomagnetic activity due to filtration requirements. Nevertheless, as Fig. 11 shows, this is possible (according to the latest installation data, the correlation of *Ub* with *Dst* is .89±0.04 with *Ub* leading *Dst* by 238 days).

While the applicability of underwater installation data for geomagnetic activity forecasts is limited, the laboratory installation serving as a reference observatory in the Baikal experiment has accumulated long series, despite also having technical interruptions here. The longest of them lasted almost 8 years (25.09.2009–15.04.2017). This allows for the correct application of various self-learning predictive algorithms, covering the most interesting range of quasi-periods from 1 to 4 years, free from both intra-annual periodicities and the main harmonics of the 11-year cycle, i.e., the range where the random component in *Dst* predominates.

Analysis showed that the global maximum correlation of *U* with *Dst* reaches 0.97 with *U* leading *Dst* by 329 days [Korotaev et al., 2024], which determines the optimal forecast lead time.

Prognostic calculations were performed using three methods. The simplest – the current regression method, is based on a piecewise linear Markov approximation, and it is the least demanding in terms of the length of the training interval. The more complex method of current impulse response characteristic, described above, is also based on a piecewise linear approximation but takes into account the non-Markov nature of the process. Finally, the neural network backpropagation method is the most labor-intensive but does not impose any restrictions on the nature of the process connection. The results of applying all three methods are shown in Fig. 12–14.

Fig. 12, Fig. 13, Fig. 14.

## 6. CONCLUSION

In a series of field experiments, a step has been made towards studying an important property of macroscopic entanglement - the backward-time response of detectors of nonlocal correlations to certain heliogeophysical processes with a large random component.

The quantitative characteristics of macroscopic nonlocal correlations in reverse time have been experimentally evaluated.

The possibility of using these correlations to forecast random variations in geomagnetic and solar activity with an accuracy , sufficient for all practical purposes, has been demonstrated.

## REFERENCES


− *Korotaev S.M., Budnev N.M., Serdyuk V.O., Zurbanov V.L., Mirgazov R.R., Shneer V.S., Machinin V.A., Kiktenko E.O., Buzin V.B., Panfilov A.I.* New results of monitoring the vertical component of the electric field in Lake Baikal using the surface-bottom setup // Geomagnetism and Aeronomy. Vol. 55. No. 3. P. 406-418. 2015. https://doi.org/10.7868/S001679401502011X

− *Korotaev S.M., Budnev N.M., Serdyuk V.O., Kiktenko E.O., Orekhova D.A* . New results of the Baikal experiment on the prognostic effect of macroscopic nonlocal correlations // Herald of Bauman Moscow State Technical University. Series Natural Sciences. No. 4. P. 56-72. 2019. https://doi.org/10.18698/1812-3368-2019-4-56-72

− *Korotaev S.M., Morozov A.N.* Nonlocality of Dissipative Processes - Causality and Time. Moscow: Fizmatlit, 216 p . 2018.

− *Korotaev S.M., Serdyuk V.O., Gorokhov Yu.V.* Prediction of geomagnetic and solar activity based on nonlocal correlations // Doklady Akademii Nauk. Vol. 415. No. 6. P. 814-817. 2007.

− *Korotaev S.M., Serdyuk V.O., Popova I.V., Gorokhov Yu.V., Kiktenko E.O., Orekhova D.A.* Experiment on long-term forecasting of geomagnetic activity based on nonlocal correlations // Geomagnetism and Aeronomy. Vol. 64. No. 1. P. 141-148. 2024. https://doi.org/10.31857/S0016794024010144

− *Amico L., Fazio R., Osterloch A., Vedral V.* Entanglement in many-body systems // Rev. Mod. Phys. V. 80. N 2. P. 517-576. 2008. https://doi.org/10.1103/RevModPhys.80.517

− *Calsamiglia J., Hartmann L., Dür W., Briegel H.-J.* Spin gases: quantum entanglement driven by classical kinematics // Phys. Rev. Lett. V. 95. N 18. ID 180502. 2005. https://doi.org/10.1103/PhysRevLett.95.180502

− *Cramer J.G.* Generalized absorber theory and Einstein-Podolsky-Rosen paradox // Phys. Rev. D. V. 22. N 2. P. 362–376. 1980. https://doi.org/10.1103/PhysRevD.22.362

− *Cramer J.G.* The transactional interpretation of quantum mechanics // Rev. Mod. Phys. V. 58. N. 3 P. 647-687. 1986. https://doi.org/10.1103/RevModPhys.58.647

− *Elitzur A.S., Dolev S.* Is there more to T? / The Nature of Time: Geometry, Physics and Perception. Eds. R. Buccery, M. Saniga, W.M. Stuckey. Dordrecht: Springer. P. 297−306. 2003. https://doi.org/10.1007/978-94-010-0155-7_31

− *Home D., Majumdar A.S.* Incompatibility between quantum mechanics and classical realism in the strong macroscopic limit // Phys. Rev. A. V. 52. N 6. P. 4959−4962. 1995. https://doi.org/10.1103/PhysRevA.52.4959

− *Hoyle F., Narlikar J.V.* Cosmology and action-at-a-distance electrodynamics // Rev. Mod. Phys. V. 67. N 1. P. 113–155. 1995. https://doi.org/10.1103/RevModPhys.67.113

− *Korotaev S.M.* Causality and Reversibility in Irreversible Time. Irvine, CA: Scientific Research Publishing, 130 p. 2011.

− *Korotaev S., Budnev N., Serdyuk V. Kiktenko E., Gorohov J., Zurbanov V.* Macroscopic entanglement and time reversal causality by data of the Baikal experiment // J. Phys. Conf. Ser. V. 1051. ID 012019. 2018a. https://doi.org/10.1088/1742-6596/1051/1/012019

− *Korotaev S., Budnev N., Serdyuk V., Kiktenko E., Orekhova D., Gorohov J.* Macroscopic nonlocal correlations in reverse time by data of the Baikal Experiment // J. Phys. Conf. Ser. V. 1557. ID 012026. 2020. https://doi.org/10.1088/1742-6596/1557/1/012026

− *Korotaev S., Budnev N., Serdyuk V., Kiktenko E., Orekhova D., Gorohov J.* Macroscopic nonlocal correlations by new data of the Baikal Experiment // J. Phys. Conf. Ser. V. 2197. ID 012019. 2022. https://doi.org/10.1088/1742-6596/2197/1/012019

− *Korotaev S.M., Gorohov J.V., Serdyuk V.O., Novysh A.V.* Response of macroscopic nonlocal correlation detector to a phase transition // J. Phys. Conf. Ser. V. 1348. ID 012041 . 2019. https://doi.org/10.1088/1742-6596/1348/1/012041

− *Korotaev S.M., Morozov A.N., Serdyuk V.O., Nalivayko V.I., Novysh A.V., Gaidash S.P., Gorohov J.V., Pulinets S.A., Kanonidi Kh.D.* Manifestation of macroscopic nonlocality in the processes of solar and geomagnetic activity // Vestnik of BMSTU. Special Issue. P. 173−185. 2005.

− *Korotaev S.M., Serdyuk V.O., Budnev N.M.* Advanced response of the Baikal macroscopic nonlocal correlation detector to the heliogeophysical processes / Unified Field Mechanics II. Eds. R.L. Amoroso, L.H. Kauffman, P. Rowlands, G. Albertini. London: World Scientific. P. 375–380. 2018b. https://doi.org/ 10.1142/9789813232044_0035

− *Kordas G., Wimberger S., Witthaut D.* Dissipation induced macroscopic entanglement in an open optical lattice // Europhys. Lett. V. 100. N 3. ID 30007. 2012. https://doi.org/10.1209/0295-5075/100/30007

− *Laforest M., Baugh J., Laflamme R.* Time-reversal formalism applied to bipartite entanglement: theoretical and experimental exploration // Phys. Rev. A. V. 73. N 3. ID 032323. 2006. https://doi.org/10.1103/PhysRevA.73.032323

− *Lean J.L., Brueckner G.E.* Intermediate-term solar periodicities: 100–500 days // Astrophys. J. V. 337. P. 568−578. 1989. https://doi.org/10.1086/167124

− *Lee S.-S.B., Park J., Sim H.-S.* Macroscopic quantum entanglement of a Kondo Cloud at finite temperature // Phys. Rev. Lett. V. 114. N 5. ID 057203. 2015. https://doi.org/10.1103/PhysRevLett.114.057203

− *Lloyd S., Maccone L., Garcia-Patron R., Giovannetti V., Shikano Y., Pirandola S., Rozema L.A., Darabi A., Soudagar Y., Shalm L.K., Steinberg A.M* . Closed timelike curves via postselection: theory and experimental demonstration // Phys. Rev. Lett. V. 106. N 4. ID 040403. 2011. https://doi.org/10.1103/PhysRevLett.106.040403

− *Ma X.-S., Zotter S., Kofler J., Ursin R., Jennewien T., Brukner Č., Zeilinger A* . Experimental delayed-choice entanglement swapping // Nat. Phys. V. 8. P. 479−485. 2012. https://doi.org/10.1038/nphys2294

− *Maldacena J., Susskind L.* Cool horizons for entangled black holes // Progress of Physics. V. 61. N 9. P. 781−811. 2013. https://doi.org/ 10.1002/prop.201300020

− *Megidish E., Halevy A., Shacham T., Dvir T., Dovrat L., Eisenberg H.S* . Entanglement swapping between photons that have never coexisted // Phys. Rev. Lett. V. 110. N 21. ID 210403. 2013. https://doi.org/10.1103/PhysRevLett.110.210403

− *Reid M.D., He Q.Y., Drummond P.D.* Entanglement and nonlocality in multi-particle systems // Frontiers of Physics. V. 7. N 1. P. 72−85. 2012. https://doi.org/10.1007/s11467-011-0233-9

FIGURE CAPTIONS

Fig. 1. Detector device schematic. *C* - housing (wall thickness 20 mm), *D* - dewar, *V* - vessel with electrolyte, *E* - electrodes (internal structure not shown), *T* - temperature sensor.
Materials: hatching - caprolon, double hatching - ebonite, dots - air, unhatched space - vacuum.

Fig. 2. Baikal deep-water installation. *1* - anchor; *2* - cable-rope; *3* - electronics unit; *4* - buoy line; *5* - submerged buoy; I, II - upper electrode detector; III, IV - lower electrode detector.

Fig. 3. Functions of independence and causality of the detector signal $U$ and solar radio emission flux $R$. $\tau<0$ corresponds to the delay of $U$ relative to $R$, $\tau>0$ - to advance.

Fig. 4. Correlation function of the detector signal $U$ and solar radio emission flux $R$, $\tau<0$ corresponds to the delay of $U$ relative to $R$, $\tau>0$ - to advance.

Fig. 5. Correlation function of the detector signal $U$ and geomagnetic activity *Dst*, $\tau<0$ corresponds to the delay of $U$ relative to *Dst*, $\tau>0$ - to advance.

Fig. 6. Solar activity forecast with a fixed lead time of 35 days (thin line) compared to the actual curve (bold line). The starting point of time is March 20, 1995. Root mean square forecast error $0.88 \cdot 10^{-22}$ W m$^{-2}$Hz$^{-1}$.

Fig. 7. Geomagnetic activity forecast with a fixed lead time of 35 days (thin line) compared to the actual curve (bold line). Time reference starting point September 19, 1995. Root mean square forecast error 1.7 nT.

Fig. 8. Solar activity forecast with a fixed lead time of 123 days (thin line) compared to the actual curve (bold line). Time reference starting point February 20, 2003. Root mean square forecast error $2.9 \cdot 10^{-22}$ W m$^{-2}$Hz$^{-1}$.

Fig. 9. Geomagnetic activity forecast with a lead time of 123 days (thin line) compared to the actual curve (bold line). Time reference starting point (in days) February 20, 2003. Root mean square forecast error 2.0 nT.

Fig. 10. Detector signal *Ut* qualitatively predicts the variation of solar activity *R* (relative to the average level) with a lead time of 180 days. Time reference starting point November 4, 2016.

Fig. 11. Detector signal *Ub* qualitatively predicts the variation of geomagnetic activity *Dst* (relative to the average level) with a lead time of 238 days.

Fig. 12. Forecast of *Dst* using the current regression method with a fixed lead time of 329 days (thin line) compared to the actual curve (bold line). Root mean square forecast error 0.99 nT.

Fig. 13. Forecast of *Dst* using the current impulse response characteristic method with a fixed lead time of 329 days (thin line) compared to the actual curve (bold line). Root mean square forecast error 0.40 nT.

Fig. 14. Forecast of *Dst* using the current neural network method with a fixed lead time of 329 days (thin line) compared to the actual curve (bold line). Root mean square forecast error 0.29 nT.

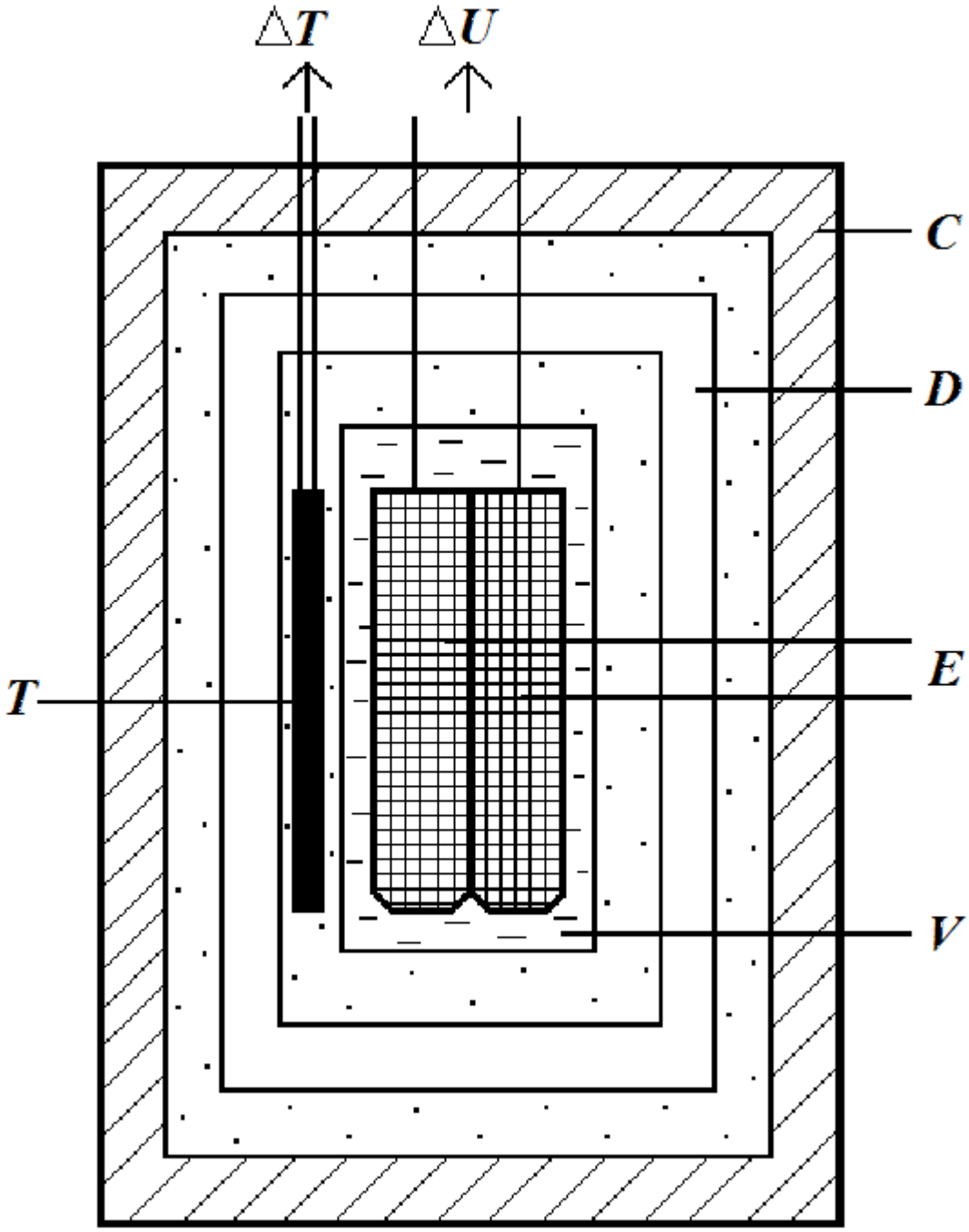


Fig. 1.

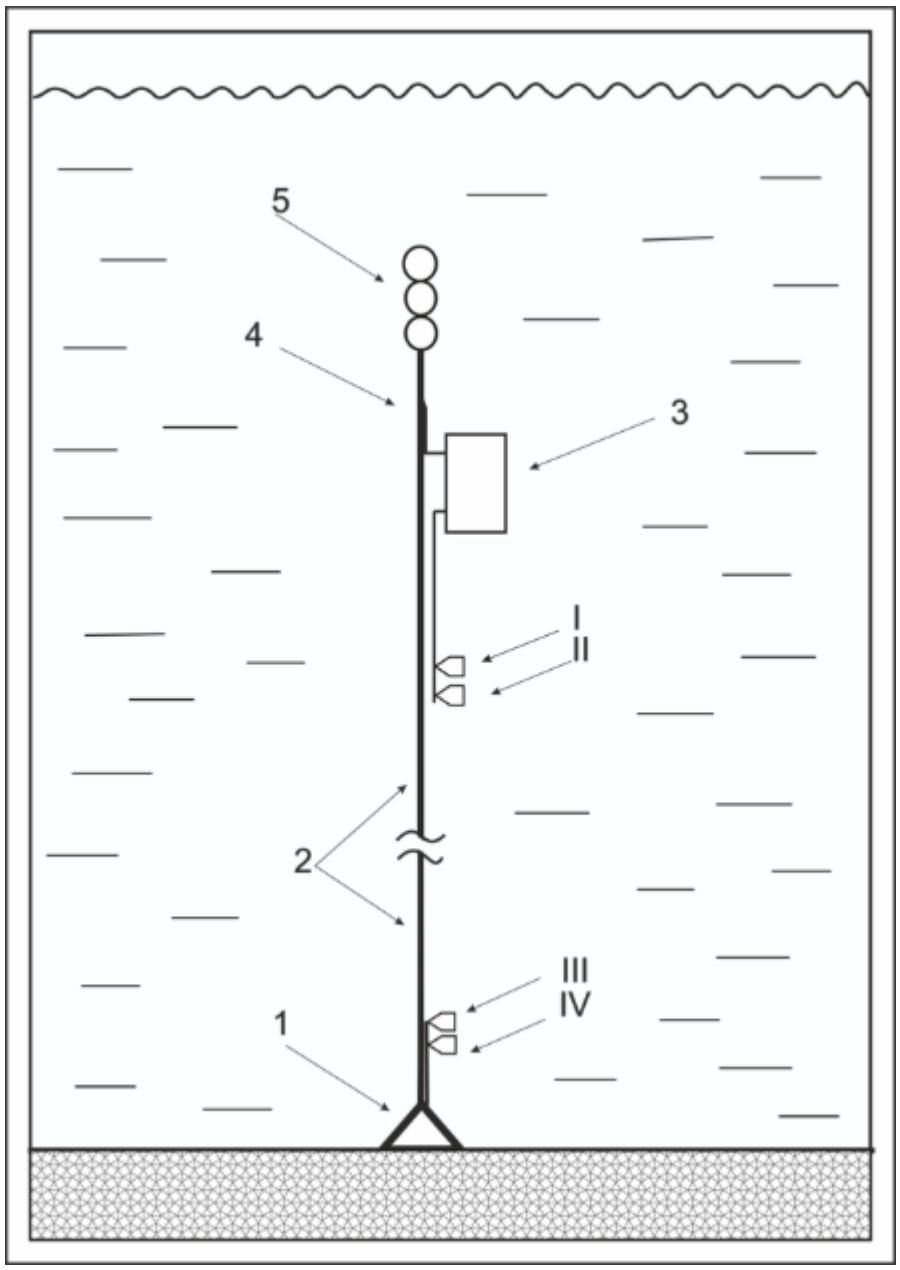


Fig. 2.

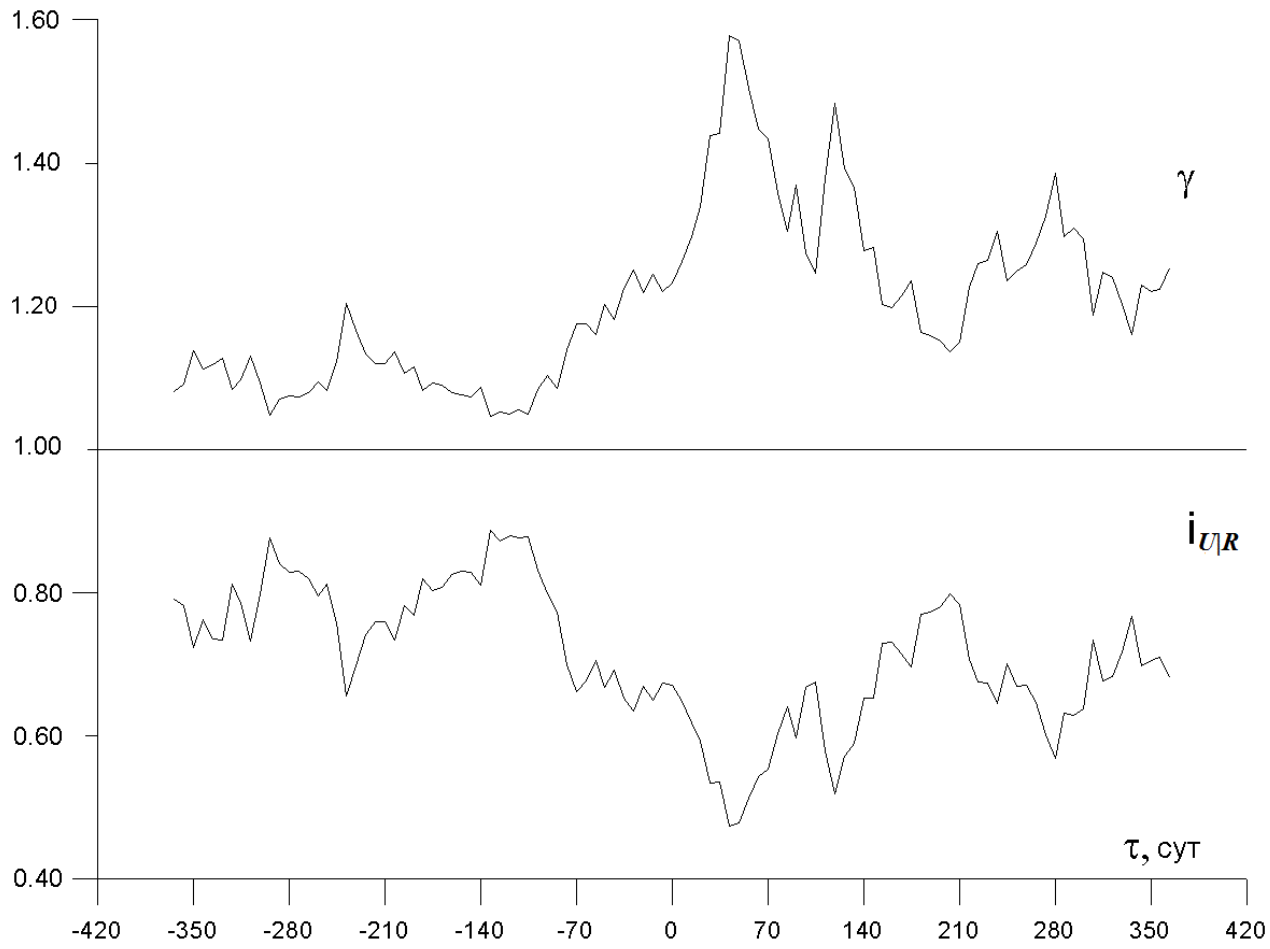
1.60
1.40
1.20
1.00
0.80
0.60
0.40
γ
i U|R
τ, сут
-420
-350
-280
-210
-140
-70
0
70
140
210
280
350
420

Fig. 3.

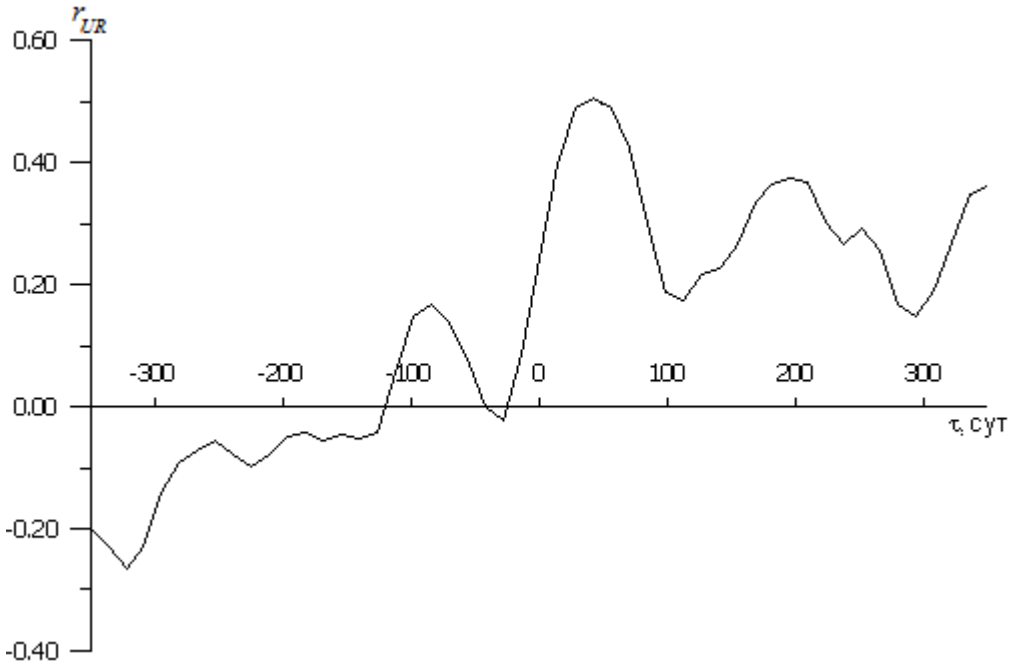
$r_{UR}$
0.60
0.40
0.20
0.00
-0.20
-0.40
-300
-200
-100
0
100
200
300
τ, сут

Fig. 4.

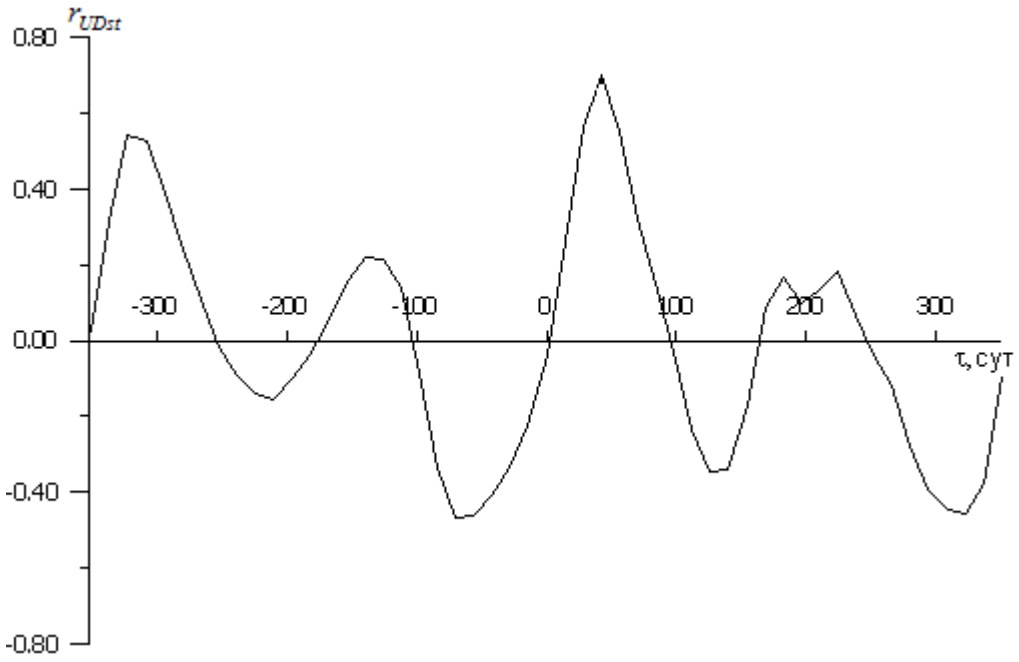
$r_{UDst}$
0.80
0.40
0.00
-0.40
-0.80
-300
-200
-100
0
100
200
300
τ, сут

Fig. 5.

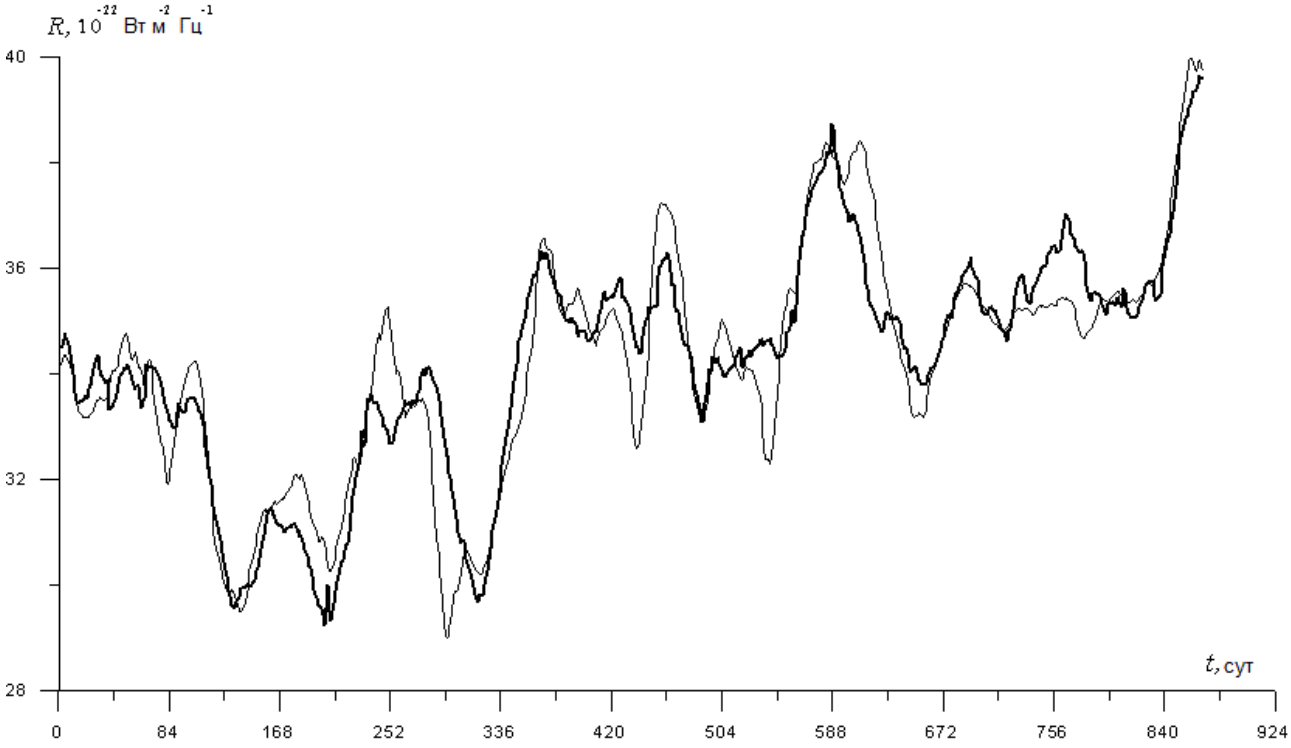
R, 10^-22 Вт м^-2 Гц^-1
40
36
32
28
t, сут
0
84
168
252
336
420
504
588
672
756
840
924

Fig. 6.

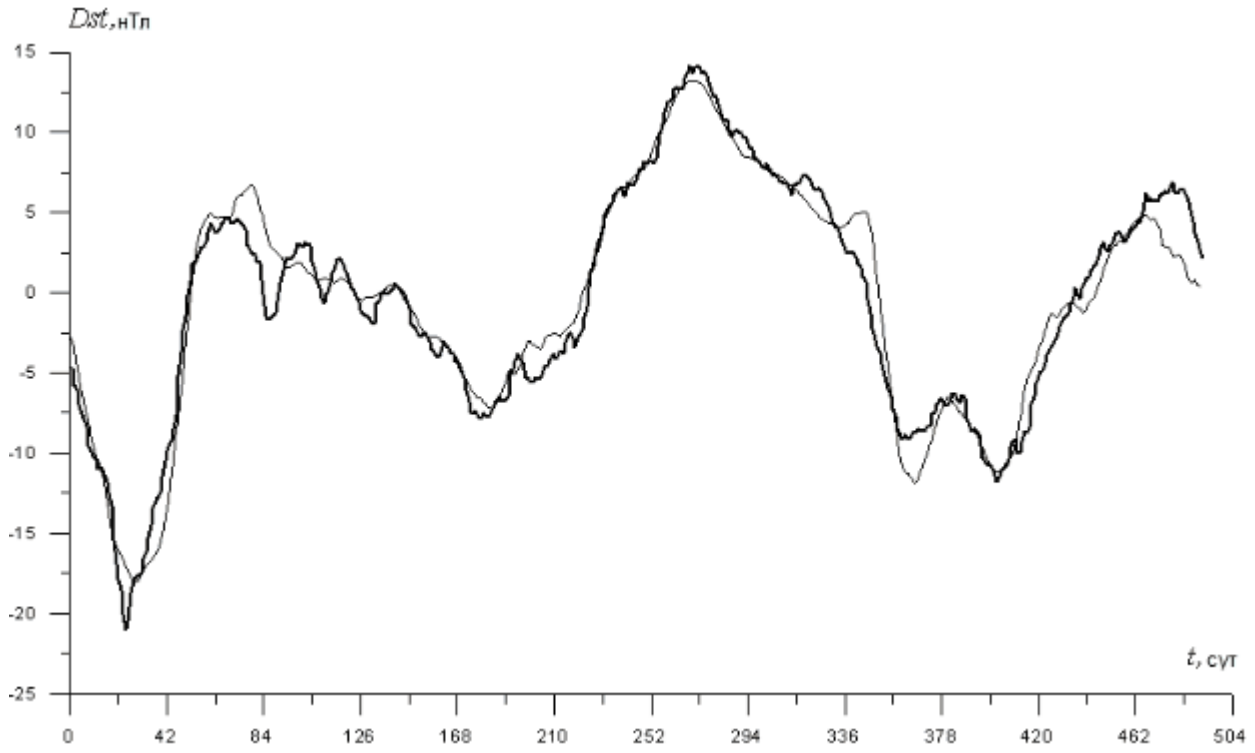
Dst, нТл
15
10
5
0
-5
-10
-15
-20
-25
t, сут
0
42
84
126
168
210
252
294
336
378
420
462
504

Fig. 7.

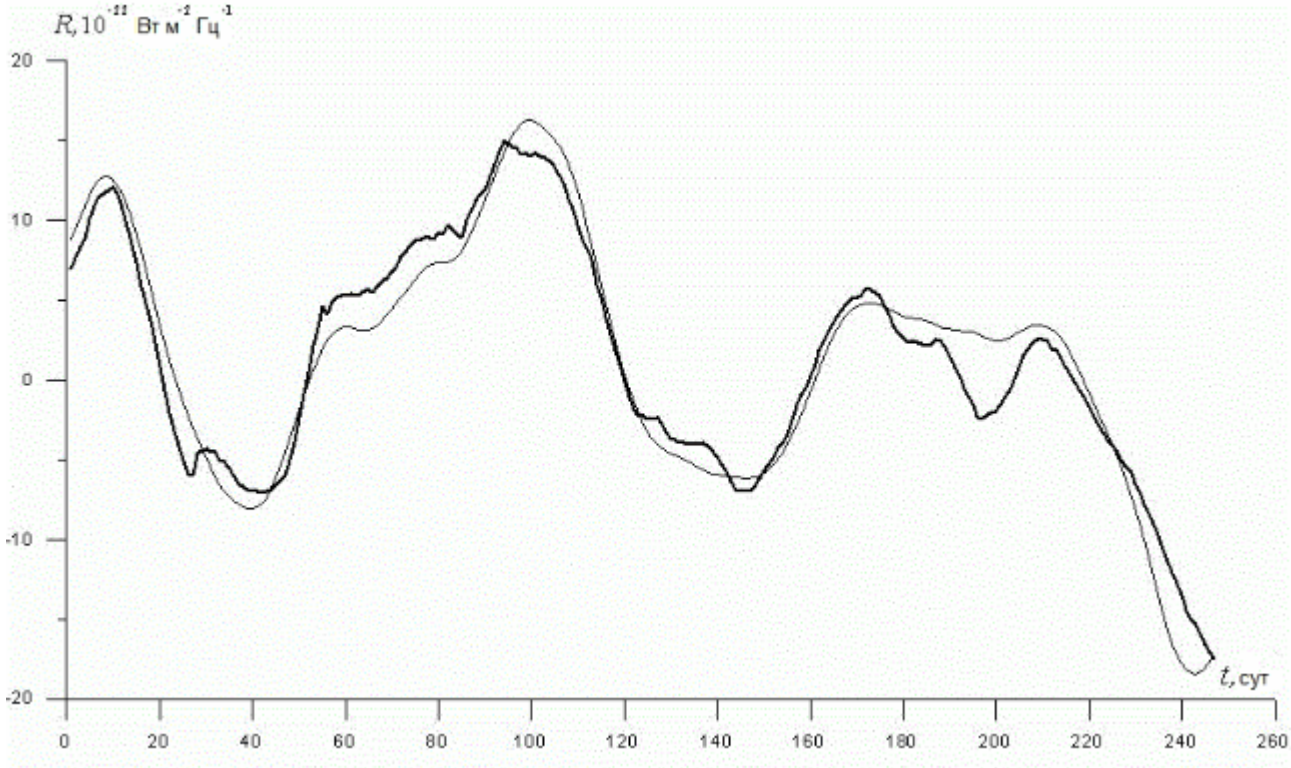
R, 10⁻¹¹ Вт м⁻² Гц⁻¹
20
10
0
-10
-20
t, сут
0
20
40
60
80
100
120
140
160
180
200
220
240
260

Fig. 8.

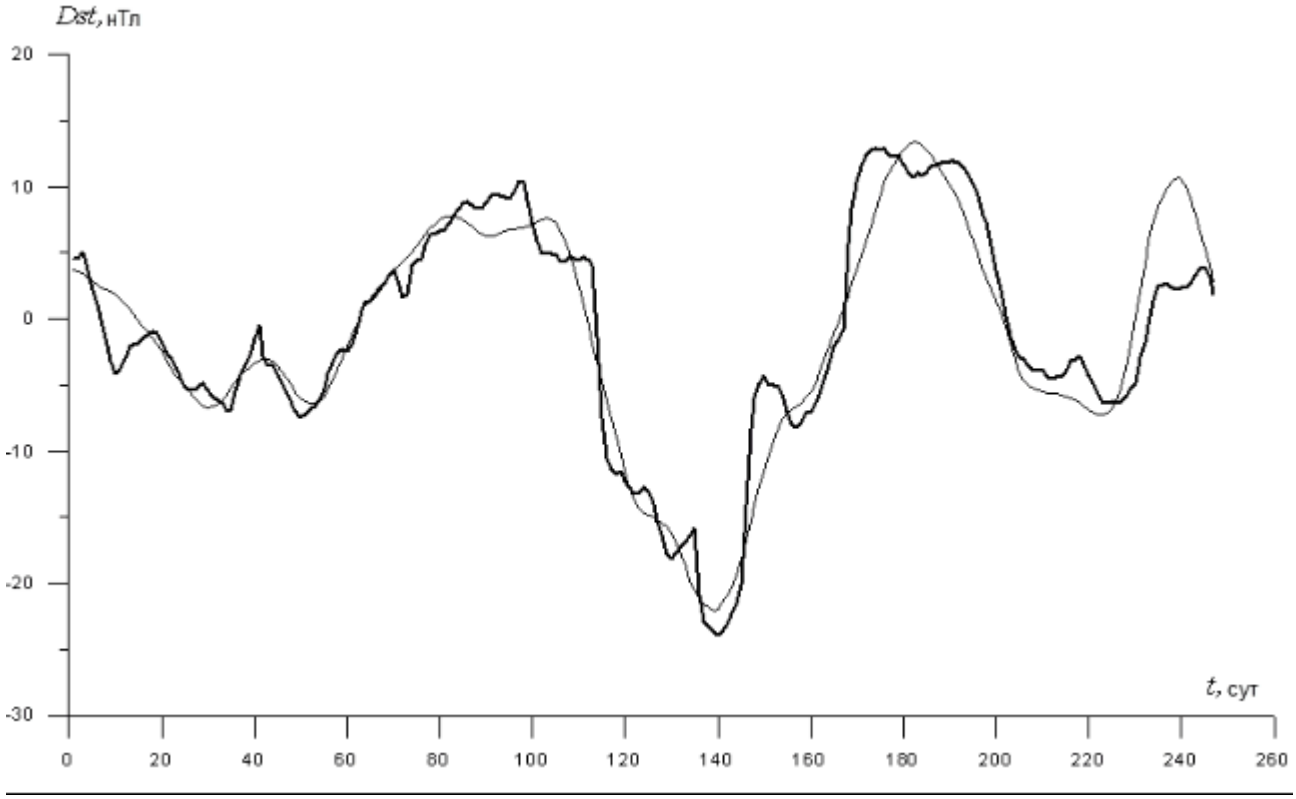
Dst, нТл
20
10
0
-10
-20
-30
t, сут
0
20
40
60
80
100
120
140
160
180
200
220
240
260

Fig. 9.

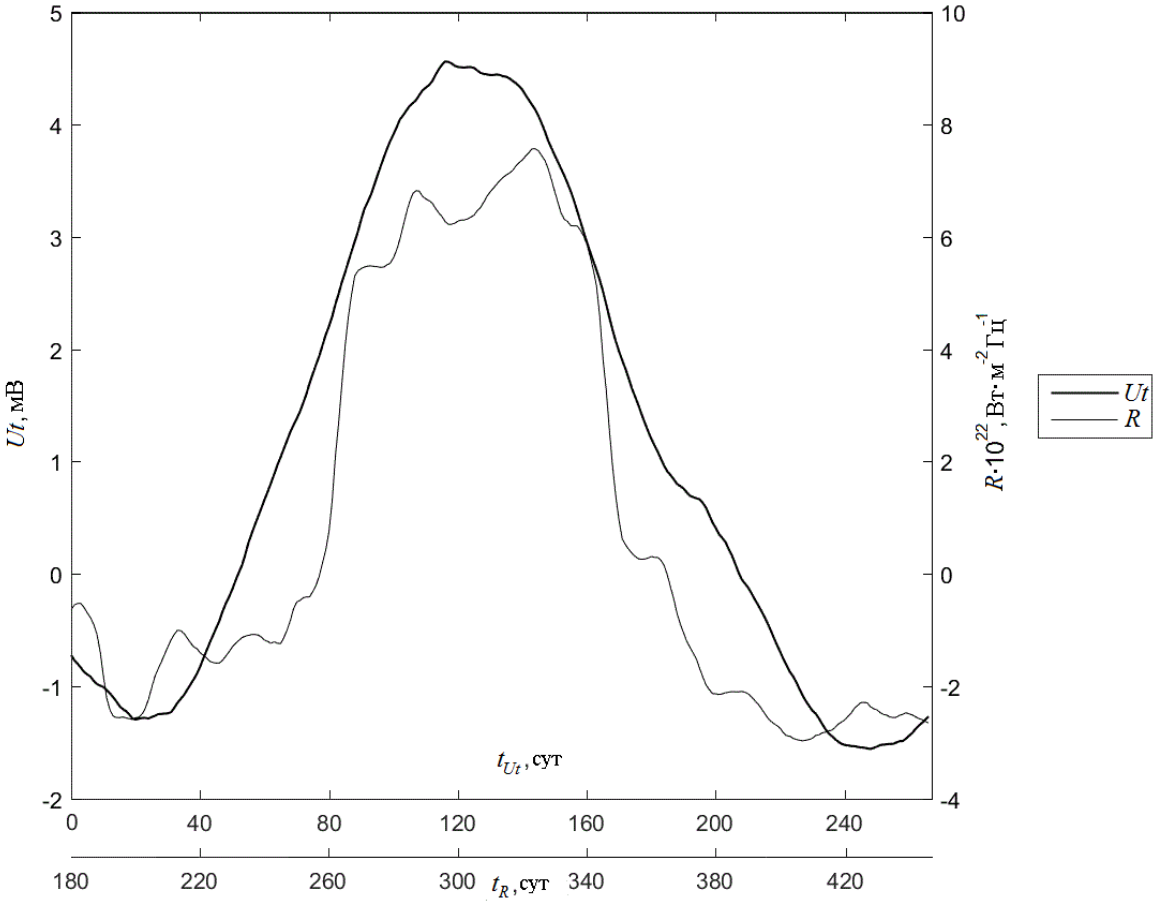
Ut, мВ
R·10^22, Вт·м^-2·Гц^-1
Ut
R
t_Ut, сут
t_R, сут
5
4
3
2
1
0
-1
-2
10
8
6
4
2
0
-2
-4
0
40
80
120
160
200
240
180
220
260
300
340
380
420

Fig. 10.

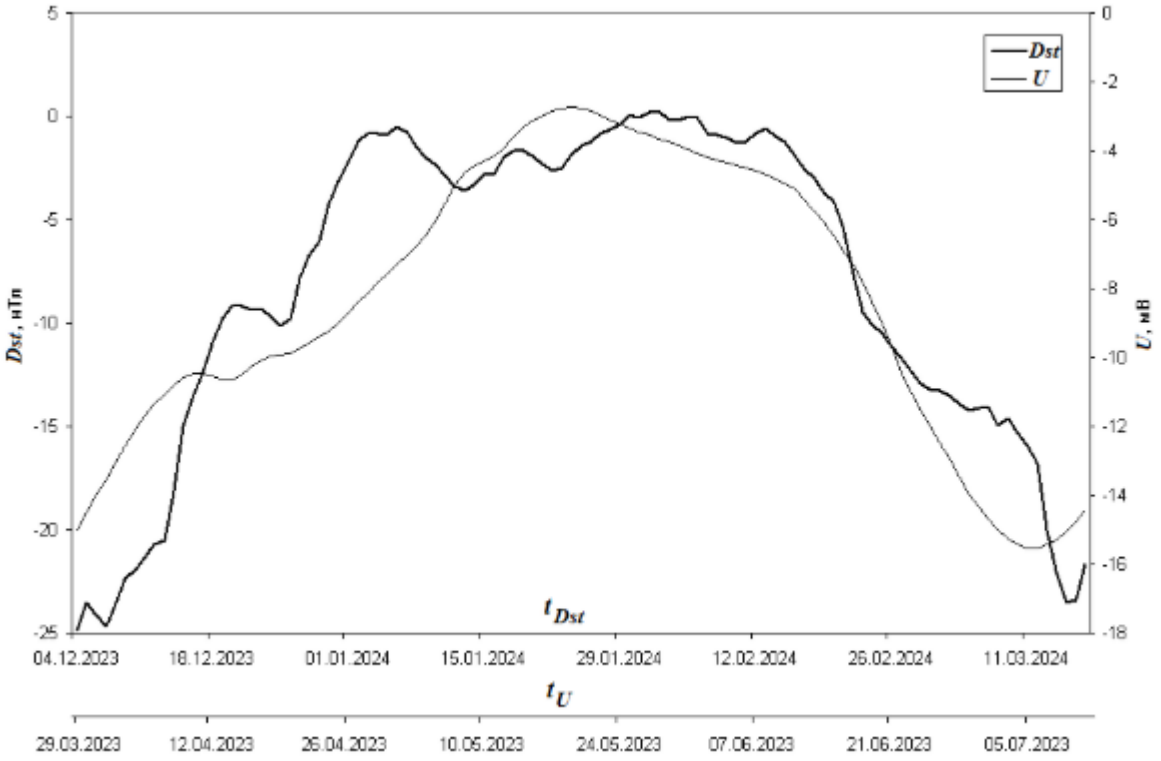
Dst
U
Dst, нТл
U, мВ
5
0
-5
-10
-15
-20
-25
0
-2
-4
-6
-8
-10
-12
-14
-16
-18
t Dst
04.12.2023
18.12.2023
01.01.2024
15.01.2024
29.01.2024
12.02.2024
26.02.2024
11.03.2024
t U
29.03.2023
12.04.2023
26.04.2023
10.05.2023
24.05.2023
07.06.2023
21.06.2023
05.07.2023

Fig. 11.


Dst, нТл
2
0
−2
−4
−6
2014-03
2014-05
2014-07
2014-09
2014-11
2015-01
2015-03
2015-05
2015-07
2015-09
2015-11

Fig. 12.

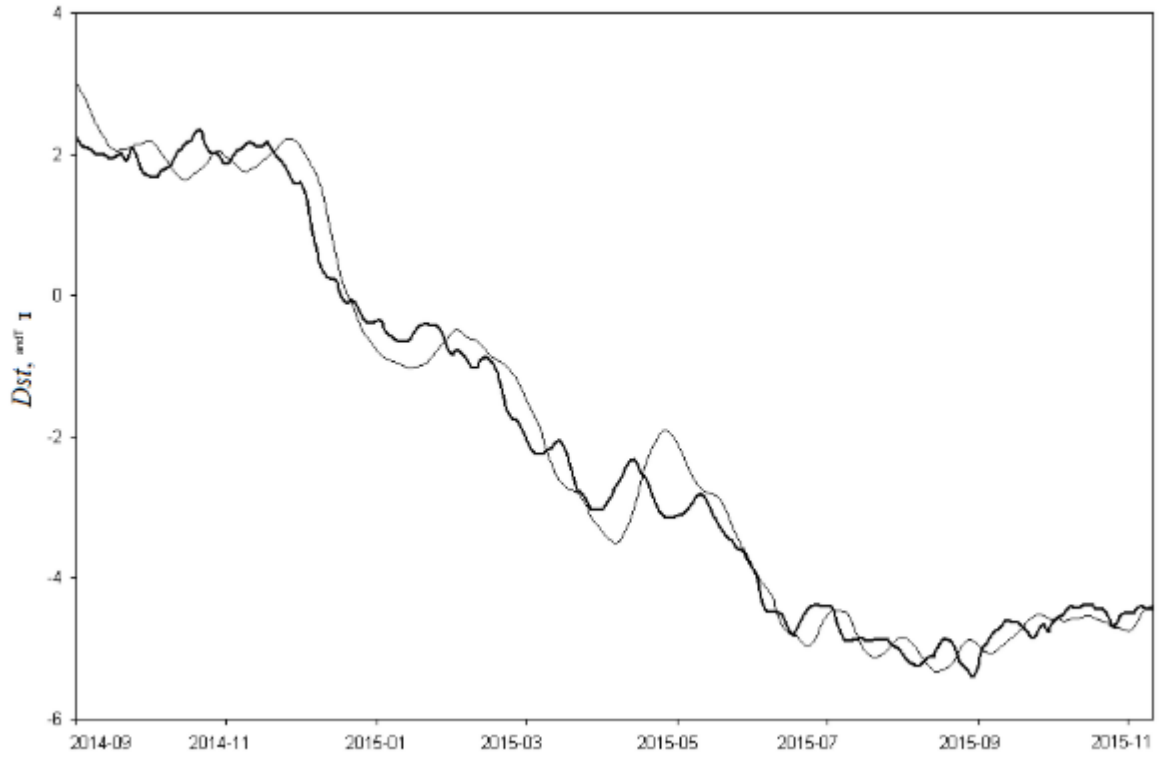
Dst, нТл
4
2
0
-2
-4
-6
2014-09
2014-11
2015-01
2015-03
2015-05
2015-07
2015-09
2015-11

Fig. 13.

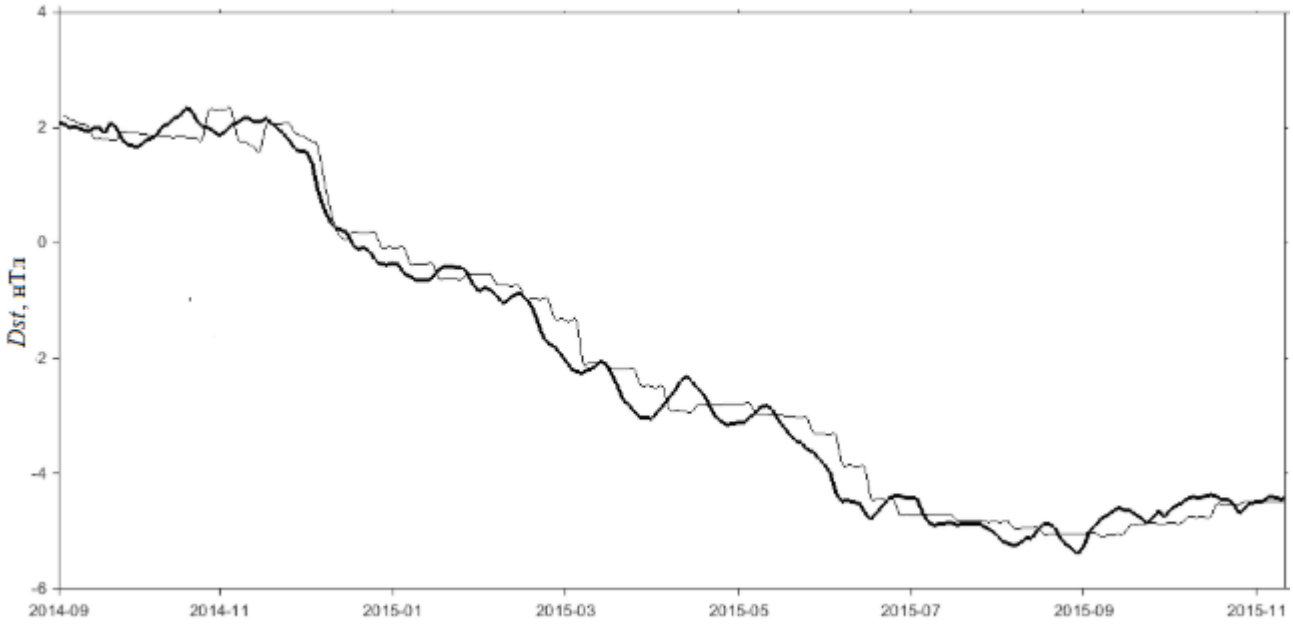
4
2
0
-2
-4
-6
Dst, нТл
2014-09
2014-11
2015-01
2015-03
2015-05
2015-07
2015-09
2015-11

Fig. 14.